Applied Catalysis B: Environmental 243 (2019) 283–293

Contents lists available at ScienceDirect

Applied Catalysis B: Environmental

journal homepage: www.elsevier.com/locate/apcatb

Construction of Pt/graphitic C_3N_4/MoS_2 heterostructures on photo-enhanced electrocatalytic oxidation of small organic molecules

Chunyang Zhai[a,1], Mingjuan Sun[a,1], Lixi Zeng[b], Mianqiang Xue[c], Jianguo Pan[a], Yukou Du[d], Mingshan Zhu[a,b,*]

[a] School of Materials Science and Chemical Engineering, Ningbo University, Ningbo 315211, PR China
[b] Guangdong Key Laboratory of Environmental Pollution and Health, School of Environment, Jinan University, Guangzhou 510632, PR China
[c] Research Institute of Science for Safety and Sustainability, National Institute of Advanced Industrial Science and Technology, Ibaraki 305-8569, Japan
[d] College of Chemistry, Chemical Engineering and Materials Science, Soochow University, Suzhou 215123, PR China

ARTICLE INFO

Keywords:
Photofunctional
Electrode
Graphitic carbon nitride
Molybdenum disulfide
Visible light
Fuel cell reaction

ABSTRACT

Low temperature fuel cells, with the features of clean, environmental friendliness, and high energy density, are considered as ideal future green energy sources. It has been recently demonstrated that the activities and stabilities of traditional fuel cell reactions can be improved by using photo-functional electrodes with assistance of light illumination. Two-dimensional (2D) heterostructure of g-C_3N_4/MoS_2 was demonstrated to be a promising photocatalyst. Herein, we used g-C_3N_4/MoS_2 nanosheets as a photo-functional substrate for the decoration of Pt nanoparticles and then applied on fuel cell electrocatalytic reactions. Comparing with traditional electrocatalytic reactions, the electrocatalytic performances of the as-synthesized Pt/g-C_3N_4/MoS_2 for the oxidation of methanol, ethanol, and formic acid upon visible light illumination are improved with 6.5, 2.2, and 2.5 times, respectively. The decisive factors in the improved catalytic performances are the synergistic effect of photo&electro-process and the effective charge separation in the designed 2D/2D g-C_3N_4/MoS_2 heterostructure.

1. Introduction

Owing to their low emission of contamination, high-energy density, and ultra-fast recharging, fuel cells have been acted as an alternative power-generation technique to convert chemical energy directly into electrical energy [1–7]. Up to date, various fuel cells such as direct methanol fuel cell (DMFC), direct ethanol fuel cell (DEFC), and direct formic acid fuel cell (DFAFC) have received great interest [1–4]. This is because those small organic molecules (SOMs) including ethanol, methanol, and formic acid have high mass energy density and easy storage and transport. In most cases, platinum (Pt) was used as the most effective electrocatalyst in the electrocatalytic oxidation of liquid fuel (*viz.* methanol, ethanol, formic acid…) [3–5]. However, due to the easy poisonous by carbonaceous intermediates together with the high cost of Pt, great efforts are still required to address the rapid increasing energy demands.

Accordingly, extensive efforts have been done to develop electrocatalysts supports to improve the performance of electrode. On one hand, the Pt electrocatalysts can be dispersed well on the surfaces of supports, which increases the catalytic active sites. Moreover, such supports also decrease the usage amount of Pt, contributing to the low-cost of electrodes. On the other hand, these supports have co-catalytic properties such as adsorption ability. Currently, semiconductor materials have been certified as candidates of electrocatalysts carriers. We all have known that these semiconductors are used as photocatalysts and have powerful oxidation ability after light irradiation. Therefore, a novel photo-enhanced fuel cell system was constructed, in which the SOMs could be oxidized by synergistic effect of electro&photo-catalytic process on a metal/semiconductor electrode upon light irradiation [6–16]. With the assistance of light irradiation, the activities and stabilities of traditional fuel cell reaction for SOM oxidation at ambient environment were greatly improved [6,7].

More recently, ultrathin two dimensional (2D) semiconductor material has received considerable attention in the field of artificial photosynthesis because of their origin 2D structural features and optical properties [17–19]. 2D graphite carbon nitride (g-C_3N_4) nanosheets have been used for various photocatalytic applications including organic photosynthesis, water contamination treatment and water splitting [19–25]. Nevertheless, because of the rapid recombination of photogenerated charge holes and electrons, the photocatalytic

* Corresponding author at: School of Materials Science and Chemical Engineering, Ningbo University, Ningbo 315211, PR China.
E-mail address: mingshanzhu@yahoo.com (M. Zhu).
[1] These authors contributed equally to this work.

https://doi.org/10.1016/j.apcatb.2018.10.047
Received 12 June 2018; Received in revised form 18 October 2018; Accepted 22 October 2018
Available online 28 October 2018
0926-3373/

efficiency of pure g-C_3N_4 is still far from satisfactory. Accordingly, significant efforts have been made to enhance the charges separation by coupling with the other materials [19,26,20–31]. In general, 2D/2D heterostructures are the most expected owing to the advantages of abundant coupling interfaces and large contact surface, which contribute to the improved photogenerated charges migration and enhanced the photocatalytic activity [19,26,20–31]. It is well recognized that 2D-layered transition metal disulfides (TMDs) such as molybdenum disulfide (MoS_2) has been considered as promising candidates of co-catalysts to improve the rate of charge separation in recent years [32–34]. Hence, 2D layered MoS_2 was coupled with g-C_3N_4 to construct 2D/2D heterostructures [35–39]. For example, Majima group showed that the photogenerated electrons from g-C_3N_4 can be rapid injected to MoS_2, resulting in enhanced photocatalytic activity on H_2 production [39].

However, the above efforts most focused on the applications of heterostructure of g-C_3N_4/MoS_2 on photocatalysis, and there are very few works beyond this category. To further extend the application of g-C_3N_4/MoS_2 composite, we used it as a support for the deposition of Pt electrocatalysts to fabricate Pt/g-C_3N_4/MoS_2 electrode. The as-prepared composite electrode was used as anode in the investigation of electrocatalytic oxidation of SOMs including methanol, ethanol, and formic acid for the first time. Owing to their nice visible light response, Pt/g-C_3N_4/MoS_2 showed obvious enhanced electrocatalytic performance after visible light illumination compared to electrocatalytic process and Pt decorated single-component *viz.* Pt/g-C_3N_4 and Pt/MoS_2 composites under visible light illumination. Efficient interfacial charger carrier mobility is observed in the desired 2D/2D heterostructures contributing to the great improvement of electrocatalytic activities under visible light illumination. The present results display that the construction of 2D/2D heterostructures opens new opportunity in the application of fuel cell reactions.

2. Experimental

2.1. Chemicals

Urea [$CO(NH_2)_2$, AR, CAS 57-13-6], chloroplatinic acid hexahydrate (H_2PtCl_6•$6H_2O$, AR, CAS 18497-13-7), ammonium tetrathiomolybdate [$(NH_4)_2MoS4$, AR, CAS 15060-55-6], dimethyl formamide (DMF, AR, CAS 68-12-2), sulphuric acid (H_2SO_4, AR, CAS 7664-93-9), potassium hydroxide (KOH, AR, CAS 1310-58-3), ethanol (CH_3CH_2OH, EtOH, AR, CAS 64-17-5), methanol (CH_3OH, MeOH, AR, CAS 67-56-1), and formic acid (HCOOH, AR, CAS 64-18-8) were purchased (Sinopharm Chemical, China) and were used directly without any purification.

2.2. Synthesis of g-C_3N_4, MoS_2, and heterostructure of g-C_3N_4/MoS_2

The nanosheets of g-C_3N_4 were obtained through heating the urea in the semi-closed environment [40]. In a typical experiment, urea powders (10 g) were dissolved into water (15 mL). The pH of above solution was adjusted to 4 ~ 5 by HCl and then dried at 80 °C with 12 h. The samples were put into an alumina crucible with a lid. The crucible was then put in the muffle furnace and held at 550 °C for 2 h with the heating rate of 5 °C min^{-1}.

The g-C_3N_4/MoS_2 was synthesized *via* a solvothermal method. 0.09 g g-C_3N_4 and 0.008 g ammonium tetrathiomolybdate were dispersed into 15 ml DMF under 20 min ultrasonication, and then transferred into Teflon autoclave (V: 25 mL). The above autoclave was held at 200 °C for 12 h. The powders were obtained through centrifugation and then washed by ethanol completely, and dried at 70 °C in an oven, obtaining the heterostructure of g-C_3N_4/MoS_2. The weight ratio of MoS_2 in the g-C_3N_4/MoS_2 is about 10 wt%. The different ratios of MoS_2 in g-C_3N_4/MoS_2 were synthesized through using different amounts of ammonium tetrathiomolybdate. The pure MoS_2 were prepared with same method without ammonium tetrathiomolybdate g-C_3N_4.

2.3. Preparation of Pt/g-C_3N_4, Pt/MoS_2, and Pt/g-C_3N_4/MoS_2

The Pt/g-C_3N_4/MoS_2 nanocomposite was prepared *via* a hydrothermal approach. 20 mg g-C_3N_4/MoS_2 and 0.68 ml H_2PtCl_6 aqueous solution (3.9×10^{-2} M) were dispersed into ethanol-H_2O mixtures (20 mL, vol = 1:1) under ultrasonication for 30 min. The mixtures were then transferred into Teflon autoclave (V: 25 mL). The above autoclave was held at 140 °C for 4 h and cooled down naturally. The powders were obtained *via* centrifugation and then washed by ethanol thoroughly and dried at 70 °C in an oven, obtaining the Pt/g-C_3N_4/MoS_2. The weight ratio of Pt is *ca.* 20 wt% for total mass. The Pt/g-C_3N_4 and Pt/MoS_2 were prepared with similar method that the g-C_3N_4/MoS_2 was replaced by bare C_3N_4 and MoS_2, respectively.

2.4. Preparation of Pt/g-C_3N_4/MoS_2, Pt/MoS_2, Pt/g-C_3N_4 modified electrodes

The Pt/g-C_3N_4/MoS_2 electrode was prepared through coating the Pt/g-C_3N_4/MoS_2 on a 3 mm in diameter of L-type glassy carbon electrode (GCE). Typically, Pt/g-C_3N_4/MoS_2 (2 mg) and Nafion solutions (5 wt%, 10 μL) were added into ethanol-H_2O mixtures (1 mL, vol = 1:1) with 30 min ultrasonication to get the dispersion homogeneously. After, 5 μL of the above dispersion was dispersed onto the surface of L-type GCE and dried at the ambient condition (containing 2 μg of Pt). The Pt/g-C_3N_4 and Pt/MoS_2 electrodes were prepared with same method, in which Pt/g-C_3N_4 and Pt/MoS_2 were used, respectively.

2.5. Photoelectrocatalytic measurements

The photoelectrocatalytic measurements were employed on a quartz reactor with an electrochemical workstation (CHI 660E), in which modified GCE, Pt wire, and Ag/AgCl were acted as working electrode, counter electrode, and reference electrode, respectively. The photoelectrocatalytic activity of methanol, ethanol, and formic acid was carried out by cyclic voltammetry (CV) measurements. The scan rate is 50 mV s^{-1}. Chronoamperometries (CA) of samples under visible light illumination or dark condition were measured at −0.2 V in 1 M EtOH + 1 M KOH solution. The chronopoenttiometric curves of Pt/g-C_3N_4/MoS_2 electrode were carried out at 100 μA under dark condition and visible light illumination. The photocurrent responses were measured in 0.1 M aqueous solution of Na_2SO_4 at 0.6 V. The electrochemical impedance spectroscopy (EIS) was measured in 1 M EtOH + 1 M KOH, 1 M MeOH + 1 M KOH, 0.5 M HCOOH + 0.5 M H_2SO_4 and 0.1 M Na_2SO_4, respectively. The EIS at different potentials were measured in 1 M EtOH + 1 M KOH solution over the frequency range between 0.1 and 10^5 Hz under an AC voltage amplitude of 5.0 mV.

During photoelectrocatalytic measurements, a xenon lamp (500 W) was used as light source and a 420 nm long pass filter was put before reactor.

2.6. Characterization

Transmission electron microscopy (TEM, JEOL-2100, operated at 120 kV, HAADF-STEM image and corresponding EDX elemental mapping operated at 200 kV) was used to evaluate the morphology and component of samples. X-ray photoelectron spectroscopy (XPS, JEOL JPS-9010 MC spectrometer) and X-ray diffraction (XRD, BrukerD8Focus, with Cu Kα radiation (50 kV) of wavelength λ = 1.5418 Å) were investigated to the component and phase structures of samples, respectively. The UV–vis properties of samples were carried out by using a UV–vis-NIR Spectrophotometer on LAMBDA 950 UV/Vis/NIR Spectrophotometer. The photoluminescence (PL) properties of samples were carried out by using fluorospectrophotometer (Edinburgh FLS920) with the excitation wavelength at 405 nm.

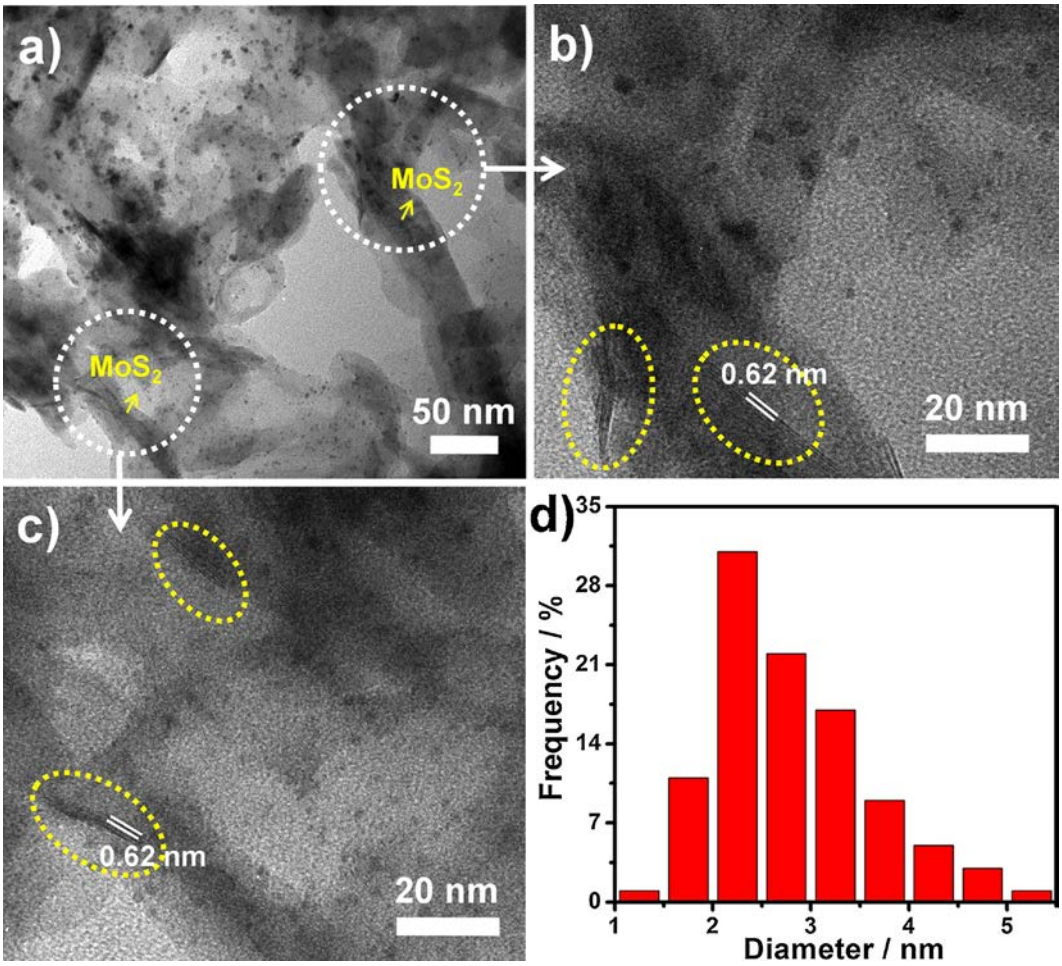

Fig. 1. TEM (a) and HRTEM (b, c) images of Pt/g-C_3N_4/MoS_2 nanocomposites. Particle size distribution histogram (d) of Pt nanoparticles on g-C_3N_4/MoS_2 from Fig. 1c and b.

3. Results and discussion

3.1. Characterization of g-C_3N_4, MoS_2, and g-C_3N_4/MoS_2 and Pt/g-C_3N_4/MoS_2

The 2D morphologies of g-C_3N_4, MoS_2, and g-C_3N_4/MoS_2 nanosheets were demonstrated by TEM. Figs. S1a and S1b show the pure g-C_3N_4 and MoS_2 with a sheet-like morphology and size range from 200 nm to 1 μm and 50 to 200 nm, respectively. After hybridized with MoS_2, small sized of MoS_2 nanosheets attached on the surface of g-C_3N_4 can be easily observed, as shown in Fig. S1c. In general, 2D sheet-like materials can be used as promising supports for the growth of metal nanoparticles. Fig. 1a shows that small nanoparticles of Pt were well decorated on the surface of g-C_3N_4/MoS_2 nanocomposites. To clear show the size of Pt nanoparticles and fine structure of MoS_2, HRTEM images of Pt/g-C_3N_4/MoS_2 from two different dotted circles in the Fig. 1a were displayed in Fig. 1b and c. Beside small particles of Pt, lattice fringes (d-spacing: 0.62 nm) were easily detected, which attributed to (002) plane of MoS_2. The average diameter of Pt decorated on g-C_3N_4/MoS_2 nanosheets is *ca.*3.0 nm, as shown in Fig. 1d. Furthermore, the pure g-C_3N_4 and MoS_2 nanosheets were also used as the substrates to deposit Pt nanoparticles, respectively. As shown in Fig. S2, similar sizes of Pt nanoparticles were observed in Pt/g-C_3N_4 and Pt/MoS_2 composites.

The HAADF-STEM image, EDX spectra, and EDX elemental mapping of Pt/g-C_3N_4/MoS_2 were provided to investigate the composition and the distribution of different elements on the surface of 2D structures. In the Fig. 2a, lots of bright dots which are Pt nanoparticles, were well dispersed on the surface of g-C_3N_4 sheets. Beside the nanosheets and bright dots, a piece of bright sheet was also detected on g-C_3N_4 sheets surface, which might be MoS_2. To confirm these conclusions, EDX at the selected zones were collected. It can be seen that the C, N, Pt, Mo, and S elements were easily detected in the Fig. 2b, while only C, N and Pt elements were found in the Fig. 2c. To further demonstrate the above phenomena, the EDX element mapping with different elements were provided, which the different components of g-C_3N_4, MoS_2 and Pt were easily observed. These results clearly show that the Pt and MoS_2 were hybridized with 2D g-C_3N_4 sheets.

To identify the elements and interaction of as-prepared samples, the X-ray photoelectron spectroscopy (XPS) of bare g-C_3N_4, MoS_2, and g-C_3N_4/MoS_2 were investigated (Fig. 3). Firstly, three peaks at 398.7, 400.2, and 401.4 eV were observed in pure g-C_3N_4, which are corresponded to C–N, tertiary nitrogen N-C3, and C-N-H groups, respectively [28,41]. Secondly, for pure MoS_2, two characteristic peaks corresponding to S $2p_{1/2}$ and S $2p_{3/2}$, and Mo $3d_{3/2}$ and Mo $3d_{5/2}$, are observed at *ca.* 163.2 and 162.0 eV, and 232.1 and 229.0 eV, respectively [27,42]. Interestingly, the binding energies of N 1s, S 2p, and Mo 3d were slightly shifted in the g-C_3N_4/MoS_2, in which the binding energies of N 1s shift to the higher binding energies while those of S 2p and Mo 3d shift to the lower binding energies, respectively. These binding energy shifts in the composites is due to the interaction of two components [41]. In the Pt/g-C_3N_4/MoS_2, beside the above elements, two peaks assigning to Pt $4f_{7/2}$ and Pt $4f_{1/2}$ were easily observed, in which at 72.0 and 75.2 eV, respectively (Fig. S3). The corresponding values are matched well with Pt (0), indicating metallic Pt nanoparticles in Pt/g-C_3N_4/MoS_2 [10,42].

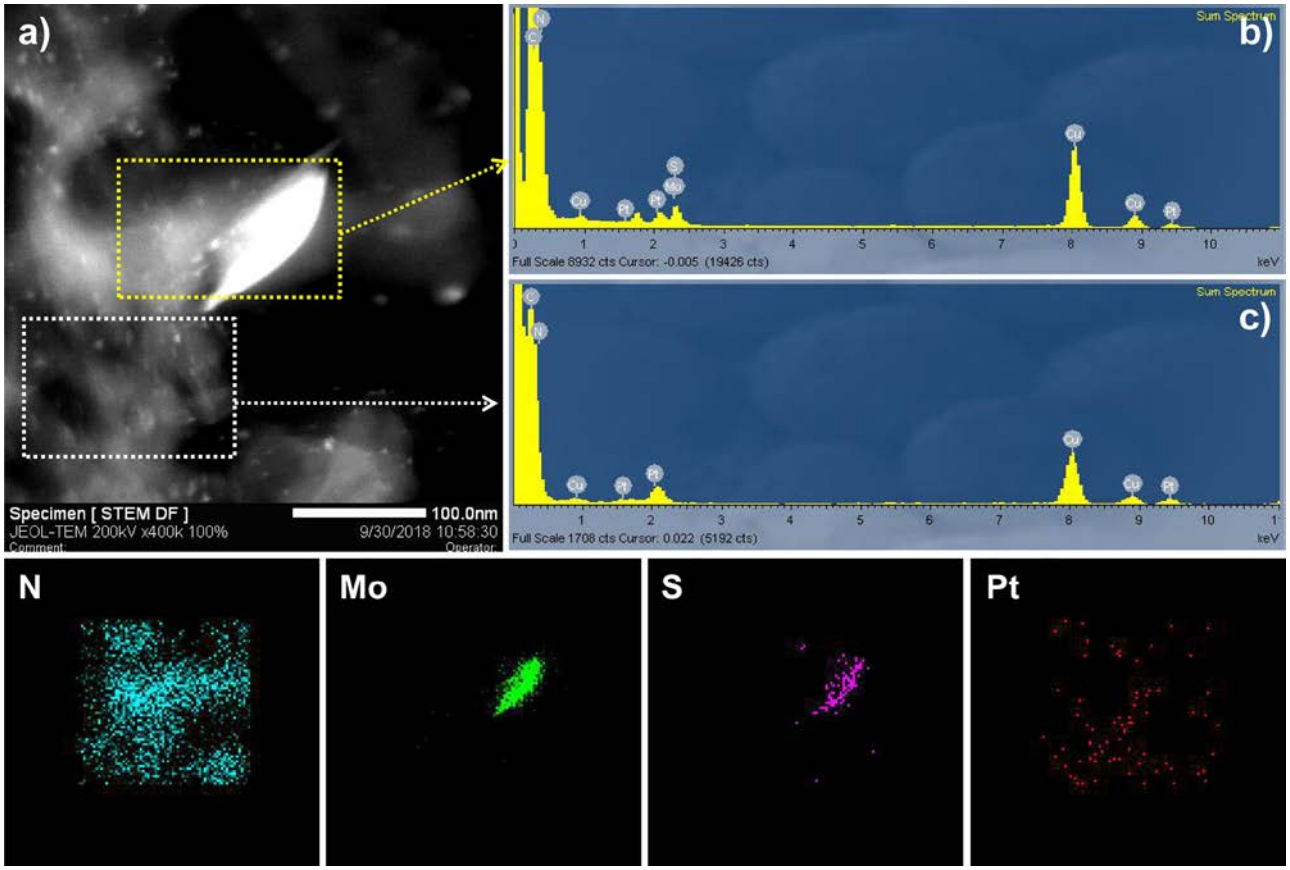

Fig. 2. HAADF-STEM image (a), EDX spectra of different areas (b and c), and element mapping of N, Mo, S, and Pt elements of Pt/g-C_3N_4/MoS_2.

XRD patterns of the as-prepared samples were measured to characterize the crystalline phases, and the results were reflected in Fig. 4A. It can be seen that all g-C_3N_4 based samples show one main characteristics peak at 27.4°, which contributes to the diffraction of (002) plane for g-C_3N_4 nanosheets [27]. For pure MoS_2, two characteristics peaks at *ca.* 32.7° and 56.7° were observed, which are contributed to the (100) and (110) crystal planes of MoS_2 (JCPDS No. 37-1492) [27]. In the composite of g-C_3N_4/MoS_2, the diffraction peaks of the MoS_2 in the g-C_3N_4/MoS_2 nanocomposites can not be observed easily, due to the low weight content of MoS_2 (5 wt%). The similar result has been reported previously by others [27]. However, when the weight content of MoS_2 is increased to 20 wt%, two small peaks can be observed at 32.7° and 56.7°, indicating the formation of g-C_3N_4/MoS_2 nanocomposites. To Pt/g-C_3N_4/MoS_2, beside the above peaks, three different peaks at *ca.* 39.7°, 46.2°, and 67.9° were detected in Pt/g-C_3N_4/MoS_2. These peaks are assigned to the (111), (200), and (220) planes of Pt [43], which further indicate the formation of metallic Pt in the composites of Pt/g-C_3N_4/MoS_2.

The optical properties of the g-C_3N_4, MoS_2, g-C_3N_4/MoS_2 and Pt/g-C_3N_4/MoS_2 were investigated by using the UV–vis diffuse reflectance spectra (UV-vis DRS). Fig. 4B shows the pure g-C_3N_4 with an absorption edge at around 452 nm, indicating that the as-prepared g-C_3N_4 has 2.7 eV band gap. Pure MoS_2 showed a broad absorption in the visible region owing to the narrow band gap. When the different MoS_2 were hybridized with g-C_3N_4 nanosheets, tailed absorptions in the far visible region were observed in the presence of MoS_2. Similar phenomena were observed in the other reports [27,29]. When Pt nanoparticles were loaded on the surface of g-C_3N_4/MoS_2, beside the absorption of g-C_3N_4 and MoS_2, an enhanced absorption was observed in the visible region due to the dark color of Pt. These visible light responses in the Pt/g-C_3N_4/MoS_2 indicate the potential advantages on photoelectrocatalytic small organic molecules under visible light illumination.

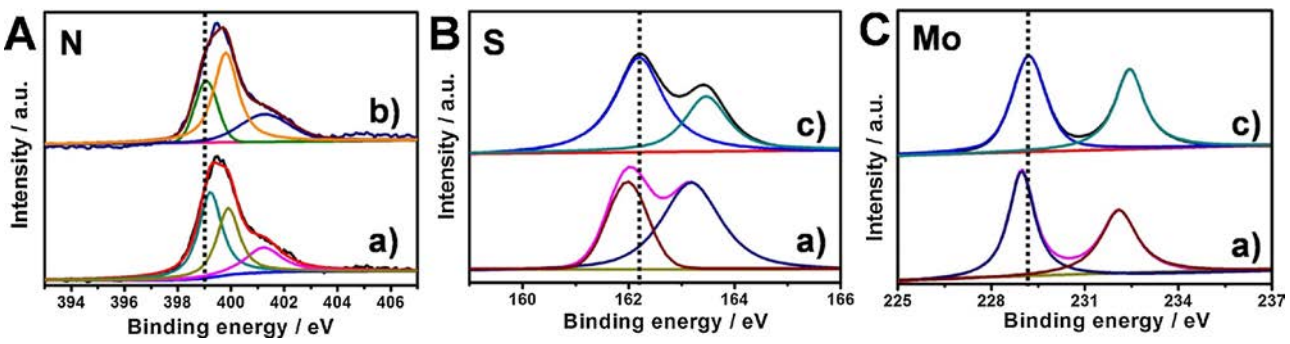

Fig. 3. XPS spectra of N 1s (A), S 2p (B), and Mo 3d (C) of the g-C_3N_4/MoS_2 (a), g-C_3N_4 (b), and MoS_2 (c).

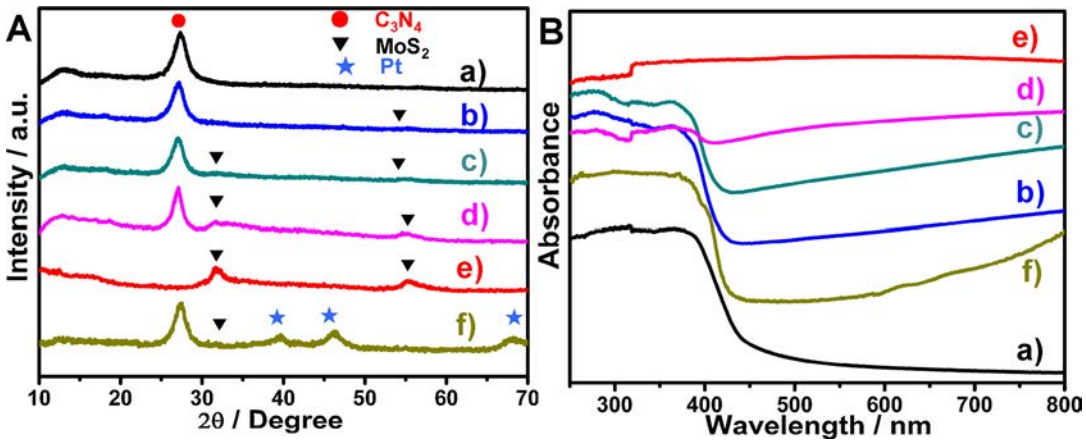

Fig. 4. XRD patterns (A) and UV-vis DRS (B) of g-C_3N_4 (a), g-C_3N_4/MoS_2 5 wt% (b), g-C_3N_4/MoS_2 10 wt% (c), g-C_3N_4/MoS_2 20 wt% (d), pure MoS_2 (e) and Pt/g-C_3N_4/MoS_2 (f).

3.2. Oxidation of ethanol on the Pt/g-C_3N_4/MoS_2 catalyst

The electrocatalytic and photoelectrocatalytic properties of the as-obtained electrodes were evaluated through catalytic oxidation of SOMs including methanol, ethanol, and formic acid, respectively. Fig. 5A shows the cyclic voltammetries (CVs) curves at the potential range from -0.9 to 0.2 V by using Pt/g-C_3N_4 and Pt/g-C_3N_4/MoS_2 as working electrodes for the electrocatalytic ethanol oxidation. There are two characteristic oxidation peaks observed at around -0.2 V in forward curve and -0.3 V in backward curve. The current density of forward peak for Pt/g-C_3N_4 is about 10.9 mA mg_{Pt}^{-1}. When the 10 wt% of MoS_2 was hybridized with C_3N_4 nanosheets, the peak current density was improved to 76.9 mA mg_{Pt}^{-1}. As comparison, the pure GCE, g-C_3N_4 and MoS_2 modified electrodes for the oxidation of EtOH displayed negligible catalytic activities (Fig. S4).

Owing to the excellent photocatalytic property of g-C_3N_4, the corresponding Pt/g-C_3N_4 and Pt/g-C_3N_4/MoS_2 electrodes were used upon visible light illumination for the oxidation of ethanol under the same conditions. As expected, the forward peak current densities of both electrodes were improved. The corresponding peak current densities were summarized in Table 1. Comparing with Pt/g-C_3N_4, the Pt/g-C_3N_4/MoS_2 was more effective towards ethanol oxidation under visible light irradiation. These results suggest that the layered MoS_2 plays a crucial role in the improvement of the electrocatalytic performance. The effects of MoS_2 ratio in Pt/g-C_3N_4/MoS_2 for photoelectrocatalytic oxidation of ethanol were measured under dark environment and visible light illumination. Fig. 5B shows that the optimum loading of MoS_2 in Pt-C_3N_4/MoS_2 was 10 wt%, in which the forward peak current densities reached 165.5 mA mg^{-1}_{Pt} under visible light illumination. Accordingly, the as-prepared Pt-C_3N_4/MoS_2 with 10 wt% of MoS_2 was used in the following experiments.

3.3. Photoelectrochemical properties of ethanol oxidation

To reveal the catalytic oxidation process of ethanol, the EIS in 1 M EtOH + 1 M KOH solution of as-prepared Pt/g-C_3N_4/MoS_2 under visible light irradiation were studied at different potential (Fig. 6). From -0.55 V to -0.25 V, the diameter of semicircle arc (DSA) was decreased with increasing potentials. In general, when the potential is below the oxidation potential (*ca.* -0.2 V), the active sites for the oxidation of ethanol are increased because of the removal of intermediate species. These intermediate species are formed from ethanol dehydrogenation at lower potential [40,44]. When the potential is above oxidation potential, the DSA was increased owing to the catalyst surface poisoning by intermediate species. Nevertheless, the arc turned to the second quadrant at -0.15 V (Fig. 6B). This is because of the removal of intermediate species from catalyst surface. Continue to increase the potentials to 0 V, the arc is gradually transferred to positive behavior (Fig. 6C), since the intermediate species were absent [40,44].

To confirm the photo-assisted electrocatalytic process on Pt/g-C_3N_4/MoS_2, different scan rates on the photoelectrocatalytic oxidation of ethanol with and without visible light illumination were carried out (Fig. 7). Firstly, the peak current densities of electrode were increased with the scan rates increase. Fig. 7B and D show a linear relation between the peak current density (i_p) and square root of scan rate ($\nu^{1/2}$) under dark condition and visible light illumination. The diffusion

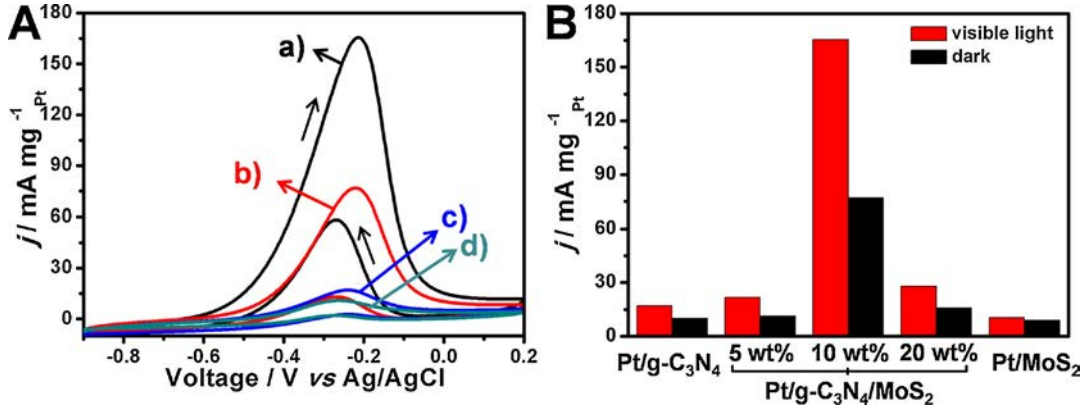

Fig. 5. A: CVs curves of Pt/g-C_3N_4/MoS_2 (a and b) and Pt/g-C_3N_4 (c and d) in 1 M EtOH + 1 M KOH solution with (a and c) and without (b and d) visible light illumination. B: Different electrodes for the oxidation of EtOH under visible light and dark environment.

Table 1
The forward peak current densities on different electrodes under visible light illumination and dark environment.

Catalyst	Pt/g-C_3N_4 (mA mg^{-1}_{Pt})				Pt/MoS_2 (mA mg^{-1}_{Pt})				Pt/g-C_3N_4/MoS_2 (mA mg^{-1}_{Pt})			
	Visible light		Dark		Visible light		Dark		Visible light		Dark	
	j	Error	*j*	Error	*j*	Error	*j*	Error	*j*	Error	*j*	Error
Methanol	163.1	± 1.5%	97.3	± 1.1%	441.7	± 0.9%	190.8	± 3.4%	1618	± 2.2%	250.5	± 4.5%
Ethanol	17.5	± 4.4%	10.9	± 2.6%	10.5	± 3.5%	6.07	± 4.4%	165.5	± 1.0%	76.9	± 2.3%
Formic acid	281.3	± 1.9%	182.8	± 2.1%	193.7	± 2.2%	50.3	± 4.1%	1557	± 0.3%	624	± 1.7%

coefficient (*D*) of electrode is calculated by Eq. (1):

$$\frac{D_{light}}{D_{dark}} = \left[\frac{(\frac{i_p}{v^{1/2}})_{light}}{(\frac{i_p}{v^{1/2}})_{dark}}\right]^2 \quad (1)$$

From Eq. (1), the value of D_{light}/D_{dark} is 2.7, which indicates the improved electron transfer kinetics at the surface of Pt/g-C_3N_4/MoS_2 and thereby contributes to the higher catalytic activity under visible light irradiation [45,46].

In general, the effective interfacial charger transfer between two components contributes to an enhanced photocatalytic performance in the composites. To investigate the photoelectric properties of Pt/g-C_3N_4/MoS_2 electrode in 1 M EtOH + 1 M KOH media, the electrochemical impedance spectrum (EIS) and linear sweep voltammetry (LSV) of Pt/g-C_3N_4 and Pt/g-C_3N_4/MoS_2 were carried out. Fig. 8A shows that the DSA of Pt/g-C_3N_4 is larger than Pt/g-C_3N_4/MoS_2. Moreover, upon visible light irradiation, both of DSAs turned to smaller than those under dark condition. Usually, the smaller DSA means smaller impedance between catalysts and electrolyte and faster interfacial charge transfer on the electrode. These results suggest the decreased internal resistances and facilitated charge transfer in the composites of Pt/g-C_3N_4/MoS_2 and those electrodes upon light illumination [47–59].

In addition, the LSV behaviors of above electrodes in the same electrolyte were also investigated with and without visible light irradiation. Fig. 8B shows that the onset potentials on the Pt/g-C_3N_4/MoS_2 and Pt/g-C_3N_4 electrodes under visible light illumination were negatively shifted by comparing with those electrodes under dark condition. The current densities of Pt/g-C_3N_4/MoS_2 and Pt/g-C_3N_4 electrode were 122 and 17.5 mA mg^{-1}_{Pt} under visible light illumination at potential of -0.3 V, which are 2.7 and 1.9 times higher than the corresponding electrodes under dark condition, respectively. These enhanced current densities are due to the improved charger mobility in the composites of g-C_3N_4/MoS_2 under light excitation.

3.4. Oxidation of methanol and formic acid on Pt/g-C_3N_4/MoS_2 catalyst

To further prove the Pt-C_3N_4/MoS_2 can be acted as a promising electrocatalyst towards small organic molecules under visible light illumination, methanol and formic acid were also investigated. The CVs for the electrocatalytic oxidation of methanol and formic acid were shown in Fig. 9and the forward peak current densities of Pt-C_3N_4/MoS_2 in different substrates solutions were summarized in Table 1. Compare to dark condition, the peak current densities of electrode were improved 6.5 and 2.5 times in the photoelectrocatalytic oxidation of methanol and formic acid, respectively. The error was below 5% in all our experiments also can be observed.

3.5. Photoelectrochemical properties of methanol and formic acid oxidation

Similar to catalytic oxidation of ethanol, the EIS and LSV behaviors of the as-synthesized Pt/g-C_3N_4/MoS_2 electrode is also investigated in methanol and formic acid media under visible light illumination and dark environment to further reveal the advantages of light photo-illuminated process. Fig. 10A and C show that the DSAs of Pt/g-C_3N_4/MoS_2 electrodes under visible light illumination are much smaller than those under dark condition both in methanol and formic acid system. On the other hand, the LSV behaviors of electrodes demonstrated similar tendencies, which showed the onset potentials were negatively shift and the current densities were enhanced. Furthermore, different scan rates on the photoelectrocatalytic oxidation of methanol and formic acid under visible light and dark environment were investigated (Figs. S5 and S6). The diffusion coefficients (D_{light}/D_{dark}) for methanol and formic acid are 27.6 and 5.7, respectively.

3.6. Stability of Pt/g-C_3N_4/MoS_2 catalyst

The long-term stability of electrocatalyst is a crucial parameter in fuel cells. Fig. 11A shows the chronoamperometric curves of the as-synthesized Pt/g-C_3N_4/MoS_2 within 3000 s both under dark environment and visible light illumination. The electrode shows stable electrocatalytic performance in both conditions, while the current density was higher under visible light illumination than that of under dark environment, revealing superior catalytic activity in photo-illuminated process. In the chronopotentiometry spectra, the potential is gradually increased with the polarization time, indicating a better catalyst's poisoning resistance. The catalyst turns to be poisoned when the voltage

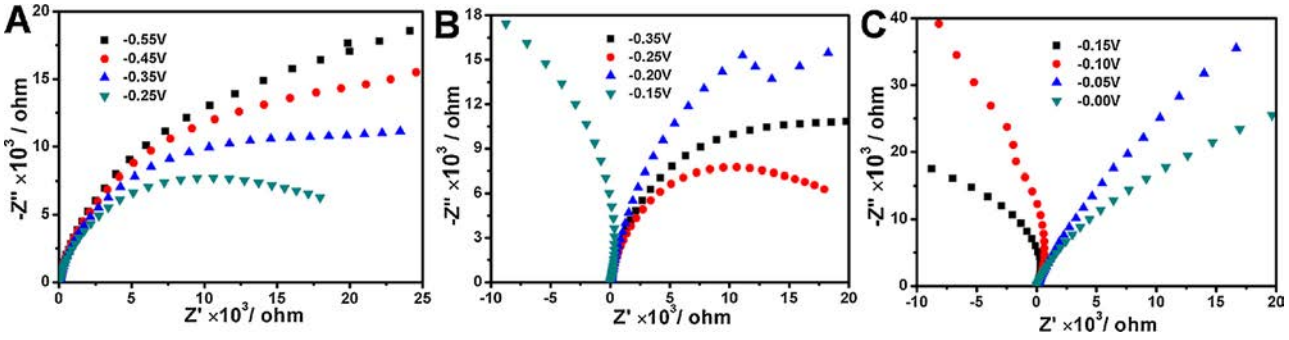

Fig. 6. EIS spectra of Pt/g-C_3N_4/MoS_2 electrode at different potentials in 1 M EtOH + 1 M KOH solution under visible light irradiation.

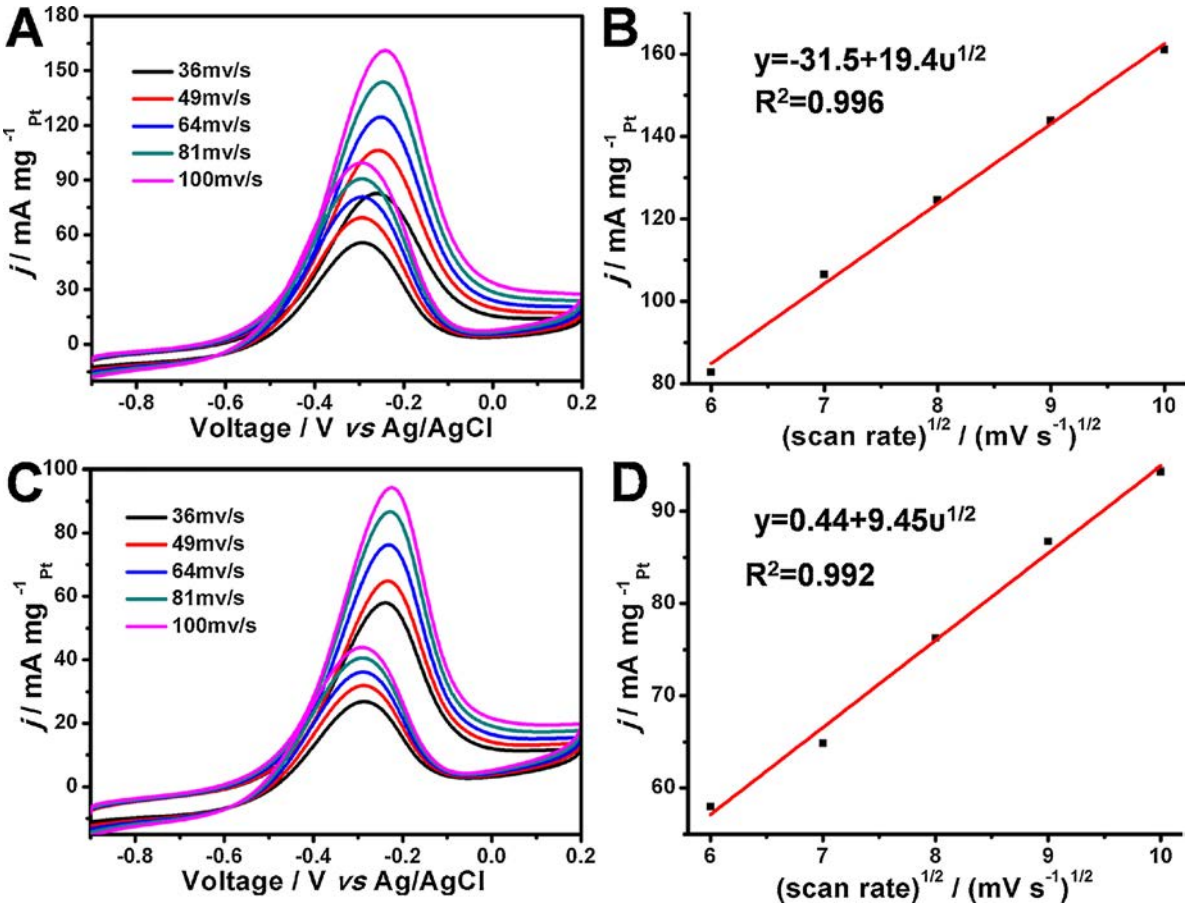

Fig. 7. A and C: CVs of Pt/g-C_3N_4/MoS_2 at different scan rate in 1 M EtOH + 1 M KOH solution. B and D: The dependence of i_p on the $v^{1/2}$. The electrode was irradiated by visible light (A and B) and under dark (C and D) condition.

increased rapidly [50]. Fig. 11B suggests the chronopotentiometry spectra of electrode both under dark condition and visible light illumination. When the electrode is upon irradiated by visible light, the potential of Pt/g-C_3N_4/MoS_2 electrode jumped to a much higher potential after 14,600 s, which is *ca.* 41.5 times than that of under dark environment (352 s). This result indicates Pt/g-C_3N_4/MoS_2 electrode has the better anti-poisoning ability under visible light illumination, which contributes to the higher catalytic activity. Although these intermediate carbonaceous species can be partial removed by the strong oxidative ability of radical ions, the catalysts still need to bear the intermediate carbonaceous species, which poisoned the catalyst after lont-time catalytic process. It still has a long way to get a successful real application.

3.7. Photoelectrochemical properties of Pt/g-C_3N_4/MoS_2 catalyst

Above results solidly demonstrated that the as-prepared Pt/g-C_3N_4/MoS_2 electrode is an efficient photoelectrocatalyst for the oxidation of small organic molecules with assistance of visible light irradiation. In general, the photocatalytic activity is highly depending on the ratio of the photogenerated charge separation. On the other hand, in comparison with the other structures, 2D/2D heterostructures possess

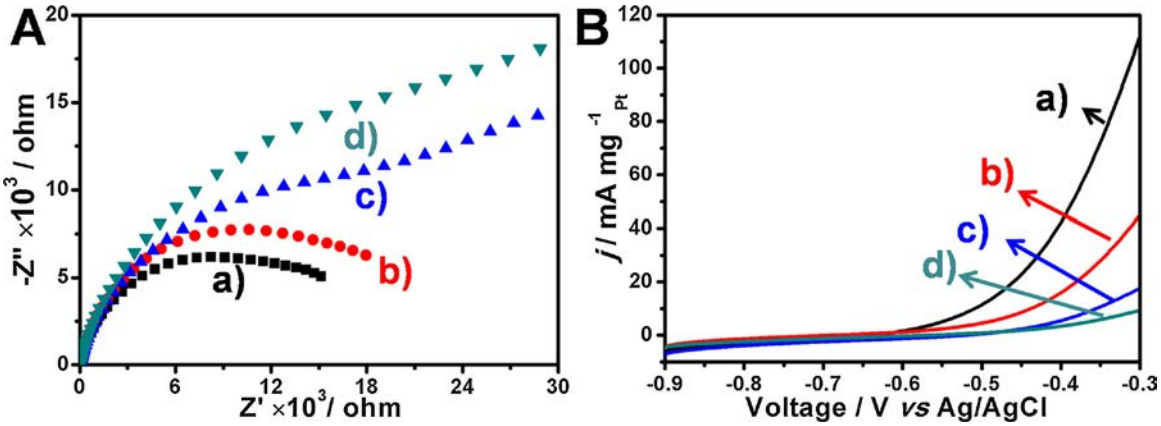

Fig. 8. The EIS (A) and LSV (B) spectra of Pt/g-C_3N_4/MoS_2 (a and b) and Pt/g-C_3N_4 (c and d) in 1 M EtOH + 1 M KOH under visible light illumination (a and c) and dark condition (b and d).

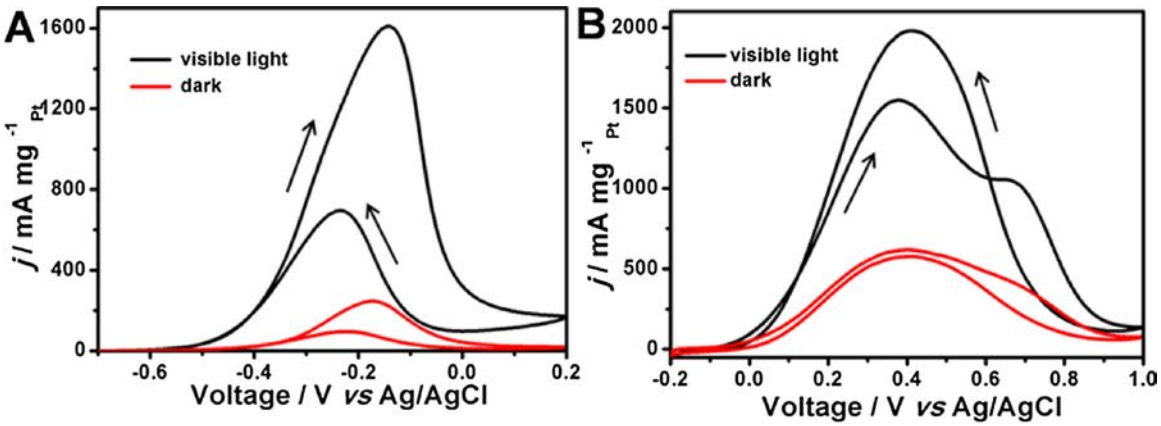

Fig. 9. CVs of Pt-C_3N_4/MoS_2 electrode in 1 M MeOH + 1 M KOH solution (A) and 0.5 M HCOOH + 0.5 M H_2SO_4 (B) under visible light illumination and dark condition.

abundant coupling interfacial sites and relative larger surface area, which facilitates migration of the photoinduced chargers more easily, thereby resulting in higher photocatalytic performance.

To confirm superior charger separation in the 2D/2D composites of g-C_3N_4/MoS_2 compare to pure g-C_3N_4, the photocurrent response together with EIS spectra of both electrodes were evaluated in Na_2SO_4 electrolyte. Fig. 12A shows *I–t* curves on the g-C_3N_4 and g-C_3N_4/MoS_2. When the working electrodes were under visible light irradiation, both electrodes showed rapid responsive photocurrents. However, compare to the pure g-C_3N_4 (0.11 μA cm^{-2}), the 2D/2D g-C_3N_4/MoS_2 composites show 6 times enhanced photocurrent intensity (0.60 μA cm^{-2}). Moreover, the photocurrent responses are repeatable during on/off cycles under visible light irradiation. Furthermore, the EIS measurements showed that the g-C_3N_4/MoS_2 under visible light illumination displays the smallest DSA than that of under dark environment and g-C_3N_4 under light irradiation and dark environment (Fig. 12B). These results clearly confirm that light irradiation promotes the electrons mobility at the surface of electrode in g-C_3N_4/MoS_2 composites.

Photoluminescence (PL) quenching is often observed due to the altered charge migration processes in the composites. The PL emission spectra together with time-resolved fluorescence decays of pure g-C_3N_4 and g-C_3N_4/MoS_2 nanocomposites were studied. As show in Fig. 13A, when the samples were excited at 405 nm, the PL emission of g-C_3N_4 showed a broad peak centered at 460 nm, which matchs its bandgap (*ca.* 2.7 eV). In the composites of g-C_3N_4/MoS_2, PL emission intensity quenching with 61.1% was detected compare to pure g-C_3N_4. The

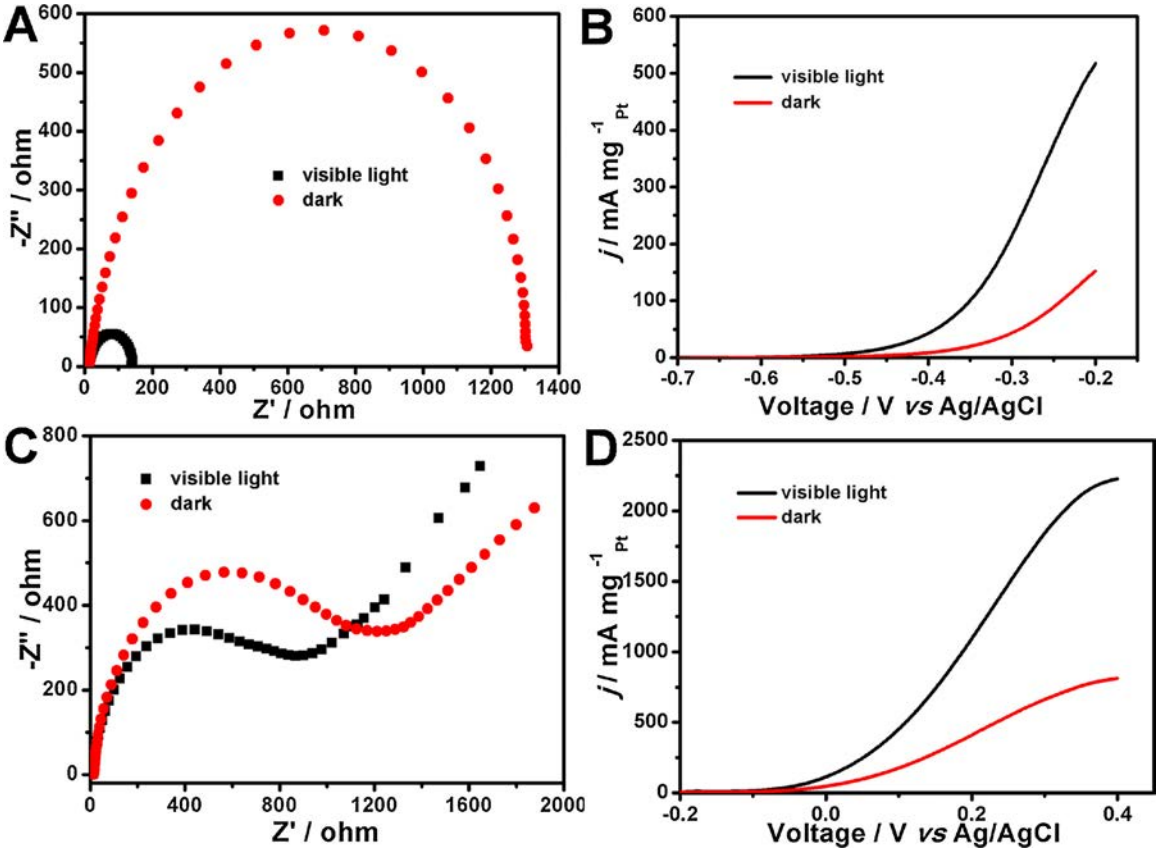

Fig. 10. The EIS (A and C) and LSV (B and D) spectra of Pt/g-C_3N_4/MoS_2 under visible light illumination and dark environment in 1 M MeOH + 1 M KOH (A and B) and 0.5 M HCOOH + 0.5 M H_2SO_4 (C and D).

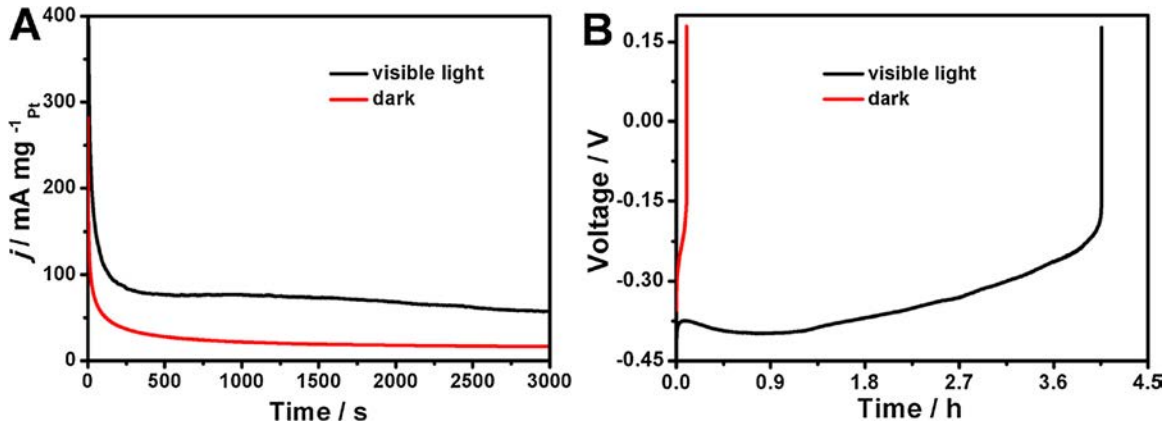

Fig. 11. Chronoamperometry (CA) at -0.2 V (A) and chronopotentiometry (CP) at 100 μA (B) of the Pt/g-C_3N_4/MoS_2 in 1 M MeOH + 1 M KOH condition under visible light illumination and dark environment.

efficient PL quenching means much less electron-hole recombination in g-C_3N_4/MoS_2 composites, indicating the photogenerated electrons from excited g-C_3N_4 were efficiently trapped by MoS_2 [11].

To probe the kinetics of electron transfer from the excited g-C_3N_4 to MoS_2, time-resolved fluorescence decay were studied, as shown in Fig. 13B and the corresponding fitted fluorescence decay data are summarized in Table 2. Pure g-C_3N_4 shows an average lifetime (τ) of 1.74 ns. In the composites of g-C_3N_4/MoS_2, the average lifetime turns to shorter. The rate of electron transfer process is calculated according Eq. (2) [51] and listed in Table 2.

$$k_{ET} = \frac{1}{\tau_{g-C_3N_4/MoS_2}} - \frac{1}{\tau_{g-C_3N_4}} \quad (2)$$

where, k_{ET} is the rate of electron transfer, $\tau_{g-C_3N_4/MoS_2}$ is the average lifetime of excited g-C_3N_4/MoS_2, and $\tau_{g-C_3N_4}$ is the average lifetime of excited g-C_3N_4. The calculated k_{ET} is *ca.* 2.8×10^8 s. This rapid electron transfer rate visually reveals an efficient electron transfer between the excited g-C_3N_4 and the MoS_2 in the composites under visible light illumination, resulting in a suppressed electron-hole recombination and thereby increased photoelectrocatalytic performance.

3.8. Proposed mechanism of photo-enhanced electrocatalytic small organic molecules oxidation on Pt/g-C_3N_4/MoS_2 catalyst

According to above results, a proposed mechanism for distinctly enhanced photoelectrocatalytic oxidation of SOMs including ethanol, methanol, and formic acid by using 2D/2D composites of Pt/g-C_3N_4/MoS_2 modified electrode was seen in Scheme 1. Firstly, in the electrocatalytic process, Pt nanoparticles deposited on the surface of g-C_3N_4/MoS_2 were acted as active sites, in which the target molecules are electro-oxidized to CO_2 on its surface. The main steps for the oxidation of methanol, ethanol, and formic acid were described as follow equations:

(1) electrocatalytic oxidation of methanol [52–54]:

$$(CH_3OH)_{solution} \rightarrow Pt\text{–}(CH_3OH)_{ads} \quad (3)$$

$$Pt\text{–}(CH_3OH)_{ads} + OH\text{–} \rightarrow Pt\text{–}HCO_{ads} + 2H_2O + e^- \quad (4)$$

$$Pt\text{–}HCO_{ads} + 2OH\text{–} \rightarrow Pt\text{–}HCOO_{ads} + H_2O + 2e^- \quad (5)$$

$$Pt\text{–}HCOO_{ads} \rightarrow Pt + CO_2 + H^+ + e^- \quad (6)$$

$$Pt\text{–}HCO_{ads} \rightarrow Pt\text{–}CO_{ads} + H^+ + e^- \quad (7)$$

$$Pt + OH\text{–} \rightarrow Pt\text{–}OH_{ads} + e^- \quad (8)$$

$$Pt\text{–}CO_{ads} + Pt\text{–}OH_{ads} \rightarrow CO_2 + 2\,Pt + H^+ + e^- \quad (9)$$

(2) electrocatalytic oxidation of ethanol: [52,55,56]

$$(CH_3CH_2OH)_{solution} \rightarrow Pt\text{-}(CH_3CH_2OH)_{ads} \quad (10)$$

$$Pt\text{-}(CH_3CH_2OH)_{ads} + 2\,OH\text{–} \rightarrow Pt\text{-}CH_3CHO_{ads} + 2H_2O + 2e^- \quad (11)$$

$$2\,Pt\text{-}CH_3CHO_{ads} + 12OH\text{–} \rightarrow 2\,Pt + 2CO_2 + 10H_2O + 12e^- \quad (12)$$

(3) electrocatalytic oxidation of formic acid: [52,57,58]
Direct oxidation processes:

$$(HCOOH)_{solution} \rightarrow Pt\text{–}(HCOOH)_{ads} \quad (13)$$

$$Pt\text{–}(HCOOH)_{ads} + OH\text{–} \rightarrow Pt\text{–}HCOO_{ads} + H_2O + e^- \quad (14)$$

$$Pt\text{–}HCOO_{ads} \rightarrow Pt + CO_2 + H^+ + e^- \quad (15)$$

Indirect oxidation processes:

$$Pt + HCOOH \rightarrow Pt\text{–}(CO)_{ads} + H_2O \quad (16)$$

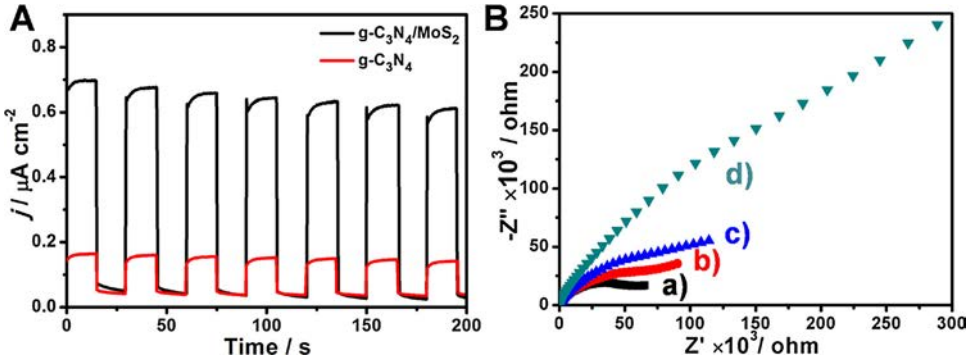

Fig. 12. Photocurrent responses (A) and EIS spectra (B) of g-C_3N_4/MoS_2 (a and b) and g-C_3N_4 (c and d) in 0.1 M Na_2SO_4 media at a potential of 0.6 V. The illumination was interrupted every 15 s in the photocurrent responses.

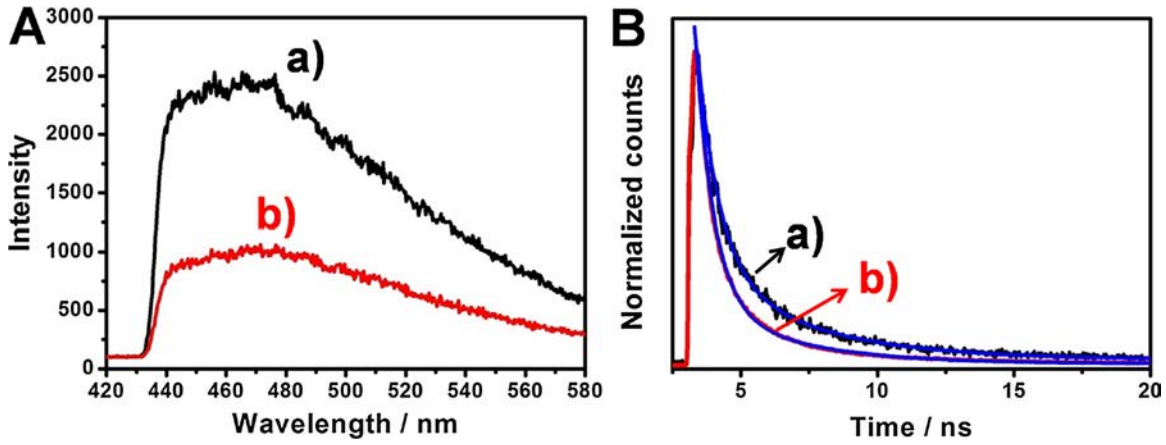

Fig. 13. PL emission spectra (A) and decay profiles (B) of the g-C_3N_4 (a) and g-C_3N_4/MoS_2 nanocomposites (b). Excitation wavelength: 405 nm.

Table 2
Time-resolved PL decay data of g-C_3N_4 and g-C_3N_4/MoS_2 derived from Fig. 13B.

Sample	τ_1 (ns)	τ_2 (ns)	τ_{ave} (ns)	k_{ET} (s^{-1})
g-C_3N_4	0.88 (73.5%)	4.12 (26.5%)	1.74	–
g-C_3N_4/MoS_2	0.67 (81.4%)	3.35 (18.6%)	1.17	2.8×10^8

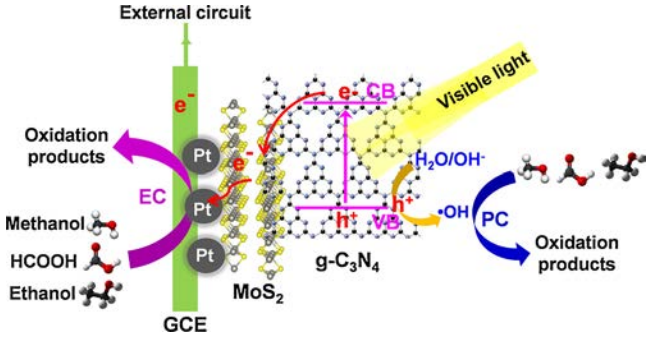

Scheme 1. Proposed scheme of the electrocatalytic (EC) and photocatalytic (PC) oxidation of small organic molecules through the Pt/g-C_3N_4/MoS_2 electrode under visible-light illumination.

$$Pt\text{–}(CO)_{ads} + Pt\text{–}(OH)_{ads} \rightarrow 2\,Pt + CO_2 + H^+ + e^- \quad (17)$$

Secondly, after Pt/g-C_3N_4/MoS_2 electrode was upon visible light illumination, the photogenerated electrons and holes were formed in the conduction band (CB) and valence band (VB) of g-C_3N_4, respectively [20–23]. The surface adsorbed OH^-/H_2O was oxidized by holes to form hydroxyl radicals (˙OHs) [11–14,47]. Then, the SOMs and intermediate carbonaceous species which adsorbed on the surface of electrocatalyst were oxidized by formed ˙OHs, leading to a photo-assisted catalytic process. This photocatalytic cleaning process for the removal of intermediate carbonaceous species promotes the poisoning suppression of catalysts, although the catalysts still need to bear the intermediate carbonaceous species after long time catalytic process. The corresponding steps are showing as follows: [59–61]

$$g\text{-}C_3N_4 + h\nu \rightarrow g\text{-}C_3N_4 + e^- + h^+ \quad (18)$$

$$h^+ + OH^- \rightarrow OH\bullet \quad (19)$$

$$CH_3OH_{ad} + OH\bullet + 5OH^- \rightarrow CO_2 + 5H_2O + e^- \quad (20)$$

$$CH_3CH_2OH_{ad} + OH\bullet + OH^- \rightarrow CO_2 + H_2O + e^- \quad (21)$$

$$HCOOH_{ad} + 2OH\text{–} \rightarrow CO_2 + 2H_2O + e^- \quad (22)$$

$$Intermediates\ (CO_{ads}) + OH\bullet \rightarrow CO_2 + H^+ + e^- \quad (23)$$

In the pure g-C_3N_4, these electron-hole pairs are recombined easily and only a small fraction of holes can be used for photocatalytic cleavage. However, in the presence of MoS_2, owing to the effective electrons transfer between g-C_3N_4 and MoS_2 [26–30], the electrons are easily injected to MoS_2 and then flow to Pt and electrode by external electric field, thereby limiting the charges recombination and improving the catalytic performance and stability.

To confirm the hydroxyl radicals (˙OHs) were generated in the samples of g-C_3N_4 and g-C_3N_4/MoS_2 during visible light illumination, electron spin resonance (ESR) spectroscopy was investigated. We used 5,5-dimethyl-1-pyrroline *N*-oxide (DMPO) as spin trapping adducts to detect the formation of ˙OH. Fig. 14 shows four-line spectra with relative intensities of 1:2:2:1 in the system of g-C_3N_4 after visible light illumination, indicating that the ˙OH can be generated in the presence of g-C_3N_4 under visible light illumination [62]. Moreover, after hybridzation of MoS_2, the signals of •OHs were improved obviously. This phenomenon further confirms that the electrons from excited g-C_3N_4 were rapidly transport to MoS_2, resulting in an effective charge separation and enhanced the catalytic performance.

4. Conclusions

In summary, 2D/2D heterostructure of g-C_3N_4/MoS_2 nanocomposite was synthesized to be a photofunctional support for Pt nanoparticles decoration. The as-prepared Pt/g-C_3N_4/MoS_2 exhibited efficient catalytic activities towards the oxidation of SOMs including ethanol,

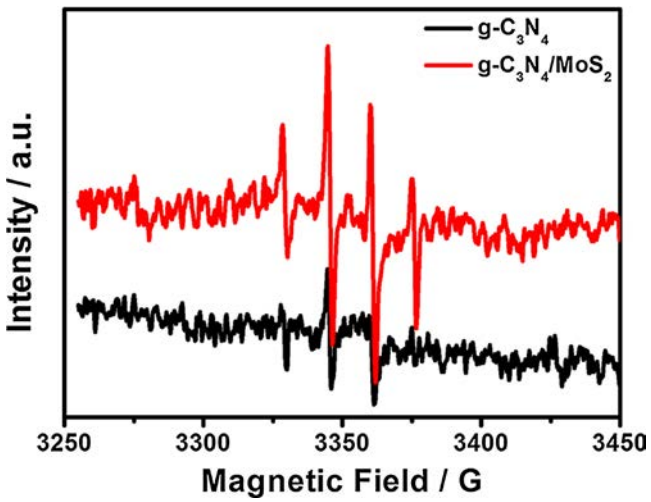

Fig. 14. ESR spectra of DMPO − OH adducts in the system of g-C_3N_4 and g-C_3N_4/MoS_2.

methanol, and formic acid. Furthermore, with the assistance of visible light illumination, the performance was distinctly improved owing to the synergistic effect of electro- and photo-process. By coupling MoS_2 nanosheets on the surface of the g-C_3N_4, the effective charger separation in the designed 2D/2D heterostructure of g-C_3N_4/MoS_2 contributes to the higher catalytic performance compared to single-component of g-C_3N_4 upon visible light irradiation. The present results suggest that the 2D/2D heterostructure of g-C_3N_4/MoS_2 are a promising photo-functional substrate in the fields of chemical and solar energy conversion.

Acknowledgments

Research was supported by the National Natural Science Foundation of China (41522304, 21577142, 21603111, and 51702173) and also supported by K.C. Wong Magna Fund in Ningbo University.

Appendix A. Supplementary data

Supplementary material related to this article can be found, in the online version, at doi:https://doi.org/10.1016/j.apcatb.2018.10.047.

References

[1] C. Bianchini, P. Kang Shen, Chem. Rev. 109 (2009) 4183–4206.
[2] F. Vigier, S. Rousseau, C. Coutanceau, J.-M. Leger, C. Lamy, Top. Catal. 40 (2006) 111–121.
[3] C. Rice, S. Ha, R.I. Masel, A. Wieckowski, J. Power Sources 115 (2003) 229–235.
[4] E. Antolini, J. Power Sources 170 (2007) 1–12.
[5] M. Cao, D.S. Wu, R. Cao, ChemCatChem 6 (2014) 26–45.
[6] M. Zhu, C. Zhai, C. Lu, Advanced Electrode Materials, Ch.11 John Wiley & Sons, Inc., Hoboken, NJ, USA, 2016, pp. 435–456.
[7] S. Sfaelou, P. Lianos, AIMS Mater. Sci. 3 (2016) 270–288.
[8] K. Drew, G. Girishkumar, K. Vinodgopal, P.V. Kamat, J. Phys. Chem. B 109 (2005) 11851–11857.
[9] M. Sun, J. Hu, C. Zhai, M. Zhu, J. Pan, Electrochim. Acta 245 (2017) 863–871.
[10] C. Zhai, M. Zhu, F. Pang, D. Bin, C. Lu, M.C. Goh, P. Yang, Y. Du, ACS Appl. Mater. Interfaces 8 (2016) 5972–5980.
[11] C. Zhai, M. Sun, M. Zhu, K. Zhang, Y. Du, Int. J. Hydrogen Energy 42 (2017) 5006–5015.
[12] A. Leelavathi, G. Madras, N. Ravishankar, J. Am. Chem. Soc. 136 (2014) 14445–14455.
[13] A. Arabzadeh, A. Salimi, M. Ashrafi, S. Soltanian, P. Servati, Catal. Sci. Technol. (6) (2016) 3485–3496.
[14] J.A. Díaz-Real, E. Ortiz-Ortega, M.P. Gurrola, J. Ledesma-Garcia, L.G. Arriaga, Electrochim. Acta 206 (2016) 388–399.
[15] Y.-H. Hsu, A.T. Nguyen, Y.-H. Chiu, J.-M. Li, Y.-J. Hsu, Appl. Catal. B Environ. 185 (2016) 133–140.
[16] C. Zhai, M. Zhu, D. Bin, H. Wang, Y. Du, C. Wang, P. Yang, ACS Appl. Mater. Interfaces 6 (2014) 17753–17761.
[17] K.S. Novoselov, A. Mishchenko, A. Carvalho, A.H. Castro Neto, Science 353 (2016) 1–11.
[18] M.-Y. Li, C.-H. Chen, Y.M. Shi, L.-J. Li, Mater. Today 19 (2016) 322–335.
[19] W.-J. Ong, Front. Mater. 4 (2017) 11.
[20] W. Jiang, W. Luo, J. Wang, M. Zhang, Y. Zhu, J. Photochem. Photobiol. C 28 (2016) 87–115.
[21] J.Q. Wen, J. Xie, X.B. Chen, X. Li, Appl. Surf. Sci. 391 (2017) 72–123.
[22] J.S. Zhang, Y. Chen, X.C. Wang, Energy Environ. Sci. 8 (2015) 3092–3108.
[23] Y. Zheng, L.H. Lin, B. Wang, X.C. Wang, Angew. Chem. Int. Ed. 54 (2015) 12868–12884.
[24] G.G. Zhang, Z.-A. Lan, X.C. Wang, Angew. Chem. Int. Ed. 55 (2016) 15712–15727.
[25] Y.D. Hou, A.B. Laursen, J.S. Zhang, G.G. Zhang, Y.S. Zhu, X.C. Wang, S. Dahl, I. Chorkendorff, Angew. Chem. Int. Ed. 52 (2013) 3621–3625.
[26] J.J. Wang, Z.Y. Guan, J. Huang, Q.X. Li, J.L. Yang, J. Mater. Chem. A 2 (2014) 7960–7966.
[27] J. Yan, Z.G. Chen, H.Y. Ji, Z. Liu, X. Wang, Y.G. Xu, X.J. She, L.Y. Huang, L. Xu, H. Xu, H.M. Li, Chem. Eur. J. 22 (2016) 4764–4773.
[28] Q. Li, N. Zhang, Y. Yang, G.Z. Wang, D.H.L. Ng, Langmuir 30 (2014) 8965–8972.
[29] J. Li, E.Z. Liu, Y.N. Ma, X.Y. Hu, J. Wan, L. Sun, J. Fan, Appl. Surf. Sci. 364 (2016) 694–702.
[30] H. Zhao, Y.M. Dong, P.P. Jiang, H.Y. Miao, G.L. Wang, J.J. Zhang, J. Mater. Chem. A 3 (2015) 7375–7381.
[31] Z.Y. Zhang, D.L. Jiang, D. Li, M.Q. He, M. Chen, Appl. Catal. B Environ. 183 (2016) 113–123.
[32] C.L. Tan, H. Zhang, Chem. Soc. Rev. 44 (2015) 2713–2731.
[33] X. Li, H.W. Zhu, J. Materiomics 1 (2015) 33–44.
[34] K. Chang, X. Hai, J.H. Ye, Adv. Energy Mater. 6 (2016) 1–21.
[35] K. Pramoda, U. Gupta, M. Chhetri, A. Bandyopadhyay, S.K. Pati, C.N.R. Rao, ACS Appl. Mater. Interfaces 9 (2017) 10664–10672.
[36] J. Li, E.Z. Liu, Y.N. Ma, X.Y. Hu, J. Wan, L. Sun, J. Fan, Appl. Surf. Sci. 364 (2016) 6 94–702.
[37] X.J. Lu, Y.L. Jin, X.Y. Zhang, G.Q. Xu, D.M. Wang, J. Lv, Z.X. Zheng, Y.C. Wu, Dalton Trans. 45 (2016) 15406–15414.
[38] S.A. Ansari, M.H. Cho, Sci. Rep. 7 (2017) 1–11.
[39] X. Shi, M. Fujitsuka, S. Kim, T. Majima, Small 14 (2018) 1–9.
[40] M.S. Zhu, C.Y. Zhai, M.J. Sun, Y.F. Hu, B. Yan, Y.K. Du, Appl. Catal. B Environ. 203 (2017) 108–115.
[41] Z.Y. Zhang, K.C. Liu, Z.Q. Feng, Y.N. Bao, B. Dong, Sci. Rep. 6 (2016) 1–10.
[42] C. Zhai, M. Zhu, D. Bin, F. Ren, C. Wang, P. Yang, Y. Du, J. Power Sources 275 (2015) 483–488.
[43] M. Zhu, Z. Li, Y. Du, Z. Mou, P. Yang, ChemCatChem 4 (2012) 112–117.
[44] C. Wang, H. Wang, C. Zhai, F. Ren, M. Zhu, P. Yang, Y. Du, J. Mater. Chem. A 3 (2015) 4389–4398.
[45] Z. Yao, R. Yue, F. Jiang, C. Zhai, F. Ren, Y. Du, J Solid State Electrochem. 17 (2013) 2511–2519.
[46] M. Sun, J. Hu, C. Zhai, M. Zhu, J. Pan, ACS Appl. Mater. Interfaces 9 (2017) 13223–13230.
[47] F. Liang, Y. Zhu, Appl. Catal. B 180 (2016) 324–329.
[48] M. Zhu, Y. Osakada, S. Kim, M. Fujitsuka, T. Majima, Appl. Catal. B Environ. 217 (2017) 285–292.
[49] M. Zhu, X. Cai, M. Fujitsuka, J. Zhang, T. Majima, Angew. Chem. Int. Ed. 56 (2017) 2064–2068.
[50] F. Ren, H. Wang, C. Zhai, M. Zhu, R. Yue, Y. Du, P. Yang, J. Xu, W. Lu, ACS Appl. Mater. Interfaces 6 (2014) 3607–3614.
[51] M. Zhu, Y. Dong, Y. Du, Z. Mou, J. Liu, P. Yang, X. Wang, Chem. Eur. J. 18 (2012) 4367–4374.
[52] M.H. Shao, Electrocatalysis in Fuel Cells: A non- and Low- Platinum Approach, Springer, London, 2013.
[53] R. Nagao, D.A. Cantane, F.H.B. Lima, H. Varela, Phys. Chem. Chem. Phys. 14 (2012) 8294–8298.
[54] Y.X. Chen, A. Miki, S. Ye, H. Sakai, M. Osawa, J. Am. Chem. Soc. 125 (2003) 3680–3681.
[55] E. Antolini, Energies 10 (2017) 1–20.
[56] M.A.F. Akhairi, S.K. Kamarudin, Int. J. Hydrogen Energy 41 (2016) 4214–4228.
[57] M.G. Hosseini, M.M. Momeni, Fuel Cells 3 (2012) 406–414.
[58] N. Mojumder, S. Sarker, S.A. Abbas, Z. Tian, V. Subramanian, ACS Appl. Mater. Interfaces 6 (2014) 5585–5594.
[59] A.Y. Ahmed, T.A. Kandiel, I. Ivanova, D. Bahnemann, Appl. Surf. Sci. 319 (2014) 44–49.
[60] M. Hamandi, G. Berhault, C. Guillard, H. Kochkar, Appl. Catal. B 209 (2017) 203–213.
[61] P. Panagiotopoulou, M. Antoniadou, D.I. Kondarides, P. Lianos, Appl. Catal. B 100 (2010) 124–132.
[62] H.H. Ji, F. Chang, X.F. Hu, W. Qin, J.W. Shen, Chem. Eng. J. 218 (2013) 183–190.